Contents lists available at ScienceDirect

# Applied Catalysis B: Environmental

# Hierarchical yolk-shell WO$_3$ microspheres with highly enhanced photoactivity for selective alcohol oxidations

Zimei Chen, Jinguo Wang*, Guangjun Zhai, Wei An, Yong Men*

*College of Chemistry and Chemical Engineering, Shanghai University of Engineering Science, Shanghai 201620, PR China*

## ARTICLE INFO

## ABSTRACT

Hierarchical WO$_3$ microspheres with controllable interior structures from solid, yolk-shell, to hollow were synthesized through sonochemical precipitation and hydrogen ion-exchange routes followed by thermal treatment. During the photocatalytic selective oxidation of aromatic alcohols to their corresponding aldehydes in aqueous medium under light irradiation with full wavelengths, the yolk-shell WO$_3$ microspheres exhibited much higher photocatalytic activity than those WO$_3$ microspheres with solid and hollow structures, respectively. This superior activity of the yolk-shell WO$_3$ microspheres can be attributed to the synergistic promoting effect of the following factors: firstly, the porous structure constructed by self-assembly of the interconnected nanosheets together with high surface area promoted the light harvesting and also facilitated the adsorption and diffusion of reactant molecules; secondly, the small crystallite size favored the rapid transfer of photoelectrons, which diminished the transfer distance of photoelectrons and thus inhibited their recombination with holes; thirdly, the yolk-shell structure enhanced light harvesting *via* multiple reflections in the yolk-shell chambers. Meanwhile, all the WO$_3$ photocatalysts displayed excellent durability against structural collapse due to the robust hierarchical structures. This work identifies the important role of yolk-shell structure played in photocatalytic selective oxidation of aromatic alcohols.

© 2017 Elsevier B.V. All rights reserved.

## 1. Introduction

Selective oxidation of alcohols to carbonyl compounds as one of the most important functional group transformations in industrial chemistry has received much attention, because carbonyl compounds such as aldehydes and ketones are widely used in fragrance, confectionary, and pharmaceutical industries [1–4]. Traditional organic reactions for selective oxidation of alcohols to carbonyl compounds not only involve environmentally harmful and corrosive stoichiometric oxidants (*e.g.* Cr and Mn salts or V$_2$O$_5$) in organic solvents, but also produce large amounts of hazardous wastes under harsh conditions (*e.g.* high temperature and pressure) [2–4]. In order to overcome these drawbacks, great efforts have been devoted to exploiting clean processes for green organic synthesis [5–9]. Recently, photocatalysis emerged as a green and promising technique for organic synthesis, which is frequently carried out in aqueous medium under mild conditions without using toxic solvents and reagents [5–9].

The photocatalyst plays the critical role in determining the photocatalytic efficiency [10–20]. Until now, most studies are focused on TiO$_2$ photocatalyst due to its advantages of earth abundance, non-toxicity, and strong stability [15–20]. Since TiO$_2$ must be irradiated by UV lights because of its large intrinsic band gap (3.2 eV), intense attention has been paid to explore visible-light activated photocatalysts [21–32]. Presently, two strategies are mainly developed to achieve visible photocatalysts: one is to design TiO$_2$ doped with metal or nonmetal elements while they usually display poor activity and durability in practical applications owning to their limited amount and easy leaching of dopants [21–24], and the other is to explore non-titania photocatalysts with instinct narrow energy gaps (*e.g.* CdS, Bi$_2$O$_3$, WO$_3$, Ag$_3$PO$_4$, and Bi$_2$WO$_6$) [25–32]. Among them, WO$_3$ has been considered as one of the most ideal candidates owning to its outstanding stable physicochemical properties and wide applications in secondary batteries, gas sensors, electrolysis, and heterogeneous photocatalysis [30–32]. Monoclinic WO$_3$ with a distorted ReO$_3$-type structure is higher stable phase than any other forms (*e.g.* orthorhombic and hexagonal) and possesses a narrow intrinsic band gap (2.6 eV) [30–36], which extends the light absorption into the visible-light region, making it more suitable for photocatalytic applications.

* Corresponding authors.
*E-mail addresses:* Jinguowang1982@163.com (J. Wang), men@sues.edu.cn (Y. Men).

In addition to achieve visible-light activated photocatalysts, the nanostructure of photocatalysts also strongly influences the photocatalytic performances [34–46]. Many studies from both theoretical prediction and experimental results demonstrate that the activity and stability are strongly related to the particle size and morphology, together with the porous structure [37–46]. For example, the small particle size together with high surface area facilitates the adsorption and diffusion of reactant molecules while crystal facet with high surface energy, e.g. (001) facet in anatase $TiO_2$ and orthorhombic $WO_3$ crystal, favors the activation of reactant molecules [7,20,33,34]. Li's group reported that $TiO_2$ with flowerlike, nanotube, hollow, and yolk-shell structures promoted the light harvesting via multiple reflections and thus enhanced the photocatalytic activity especially the yolk-shell structure [41–43,46]. After that, Quan's group investigated that PANI modified core-shell $TiO_2$ microspheres exhibited remarkable improvement in photocatalytic degradation of Rhodamine B and 4-chlorophenol due to the enhanced light harvesting via multiple reflections in the yolkshell chambers [44]. Recently, Jiang's group also exhibited the similar results in studying the N-doped yolk-shell $TiO_2$ photocatalyst for the degradation of Rhodamine B [45]. More recently, we also found that $SnS_2$-$TiO_2$ with yolk-shell structure boosted the photocatalytic efficiency in Cr(VI) reduction by synergistic promoting effect of high surface area, strong $SnS_2$-$TiO_2$ interaction, and enhanced light harvesting via multiple reflections in yolk-shell chambers [22]. Recent research interest in inorganic semiconductor photocatalysts has been extended to the hierarchical nanostructures.

Herein, hierarchical yolk-shell $WO_3$ microspheres were synthesized through hydrogen ion-exchange route followed by thermal treatment, aiming to enhance light harvesting via multiple reflections and extend light response into visible region. Meanwhile, the structural effect on photocatalytic efficiency was also systematically investigated by using hierarchical $WO_3$ microspheres with solid and hollow structures as the counterparts, respectively. As expected, the hierarchical yolk-shell $WO_3$ microspheres exhibited the highest photocatalytic activity during selective oxidation of aromatic alcohols to their corresponding aldehydes in aqueous medium under light irradiation with full wavelengths, which can be attributed to the synergistic promoting effect of the porous structure together with high surface area, small crystallite size, and enhanced light harvesting via multiple reflections in yolk-shell chambers. Moreover, all the $WO_3$ photocatalysts displayed excellent durability against structural collapse due to the robust hierarchical structures.

## 2. Experimental

### 2.1. Sample preparation

The hierarchical $WO_3$ microspheres with controllable interior structures from solid, yolk-shell, to hollow denoted as WSS, WYS, and WHS in this work, respectively, were synthesized by the modified methods according to the previous literatures [47,48]. For WSS, 4.0 mmol $Na_2WO_4\cdot2H_2O$ and 5.5 mmol oxalic acid were completely dissolved in 16 mL $H_2O$ under stirring, and then 6 mL 3.0 mol/L HCl solution was added into the above solution, which was then continuously sonicated for 1.0 h. After that, the product was collected and dried at 60 °C for 24 h, and finally calcined at 450 °C for 4.0 h to get the WSS. For WYS and WHS, the $PbWO_4$ precursor was firstly synthesized by the following route: a transparent solution containing 1.0 mmol $Na_2WO_4\cdot2H_2O$, 1.0 mmol $PbAc_2\cdot3H_2O$, 1.0 mmol CTAB, and 50 mL ethylene glycol was added into a 100 mL autoclave and kept at 160 °C for 10 h, and then the product was collected and dried at 60 °C for 2.0 h to obtain the $PbWO_4$ precursor (see Fig. S1). After

that, 1.0 mmol $PbWO_4$ was firstly immersed in 100 mL 4.0 mol/L $HNO_3$ for 12 h, and then the sample was collected and dried at 60 °C for 12 h. Subsequently, the acid-treatment sample was secondly immersed in 100 mL 4.0 mol/L $HNO_3$ for another 36 h, and then the after-treatment was the same as WSS to obtain WYS. The WHS was synthesized by the same method to WYS except that the $PbWO_4$ precursor was immersed in 100 mL 4.0 mol/L $HNO_3$ solution for 48 h by one-pot operation. The crushed yolk-shell $WO_3$ microspheres were prepared through strongly grinding WYS by hand at room temperature, and denoted as CWYS.

### 2.2. Characterization

The crystal structure and morphology were characterized by using X-ray diffraction (XRD, BRUKER D2 PHASER with Cu Kα radiation), field emission scanning electron microscopy (FESEM, Hitachi S4800), high-resonance transmission electron microscopy (HRTEM) and selected area electron diffraction (SAED) on a JEOL JEM-2100. $N_2$ adsorption-desorption isotherms were determined on Micromeritics ASAP 2460 at 77 K, from which, the surface area ($S_{BET}$), pore volume ($V_P$) and pore diameter ($D_P$) were calculated by applying Brunauer-Emmett-Teller (BET) and Barrett-Joyner-Halenda (BJH) models on the desorption branches. Photoluminescence spectroscopy (PLS), UV–vis diffuse reflectance spectra (UV–vis DRS) and Fourier-transform infrared (FTIR) spectra were collected on Varian Cary-Eclipse 500, MC-2530, and NEXUS-470, respectively. The photocurrent measurements were conducted on a self-made three-electrode quartz cell containing 30 mL 0.50 mol/L $Na_2SO_4$ aqueous solution with PAR VMP3 Multi Potentiotat apparatus and BAS Epsilon workstation, and the testing system was equipped with a 300 W xenon lamp with full wavelengths. The Pt plate and the Ag/AgCl electrode were used as the counter and reference electrodes, respectively, and the work electrode was prepared by depositing 10 mg photocatalyst onto fluoride-tin oxide (FTO) conductor glass. The photocatlytic products of selective oxidation of aromatic alcohols were detected by GC–MS (Agilent 6890N/5973I).

### 2.3. Activity test

The photocatalytic selective oxidation of aromatic alcohols were carried out at 25 °C in a self-designed 50 mL reactor (see Fig. S2) containing 0.10 g photocatalysts, 10 mL distilled $H_2O$ and 0.10 mmol benzyl alcohol or its derivatives in air atmosphere. All the photocatalytic reactions were conducted under irradiation by using a 300 W xenon lamp with full wavelengths located at 20 cm away from the reactor. After reacting 5.0 h, the reaction products were extracted with diethylether and analyzed by a gas chromatograph (Shimadzu, GC-2014C) equipped with a TB-1 column and a flame ionization detector (FID). Blank experiments demonstrated that no measurable amounts of oxidation products for aromatic alcohols occurred in the absence of either light irradiation or the $WO_3$ photocatalyst. The capturing experiment of active species was also conducted by the same method except addition of different scavengers with amount of 40 mmol. The reproducibility of all the activity tests was checked by repeating each result at least three times and found to be within acceptable limits (±3.0%).

## 3. Results and discussion

### 3.1. Structural characteristics

The XRD patterns in Fig. 1 demonstrated that all the $WO_3$ samples were present in monoclinic phase with high crystallization degree, corresponding to the 2θ at 23.1°, 23.6°, 24.4°, and 26.6° indicative of the (002), (020), (200), and (120) diffractions (JCPDS

**Table 1**
Physical structural parameters and special photoactivity of different samples.

| Sample | $S_{BET}$ (m$^2$ g$^{-1}$) | $V_p$ (cm$^3$ g$^{-1}$) | $D_p$ (nm) | Crystallite size (nm) | Special photoactivity[a] (mol m$^{-2}$ h$^{-1}$) |
|--------|------|-------|----|----|-------------------|
| WSS | 13 | 0.096 | 31 | 29 | $2.37 \times 10^{-6}$ |
| WYS | 17 | 0.099 | 22 | 25 | $7.47 \times 10^{-6}$ |
| WHS | 15 | 0.089 | 22 | 27 | $4.75 \times 10^{-6}$ |
| CWYS | 18 | 0.119 | 26 | 25 | $2.35 \times 10^{-6}$ |

[a] Benzyl alcohol conversion amount per unit surface area of catalysts after reacting 5.0 h.
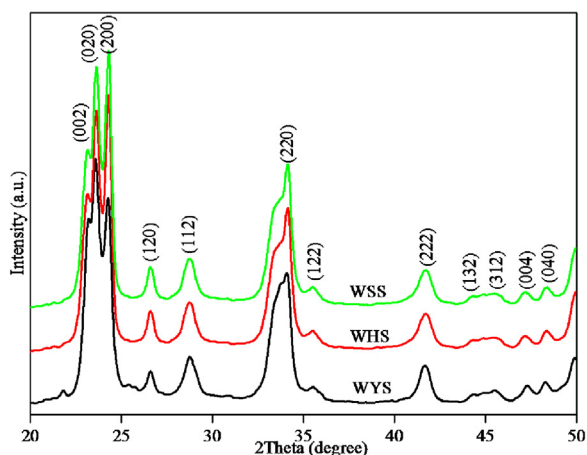


**Fig. 1.** XRD patterns of different samples.
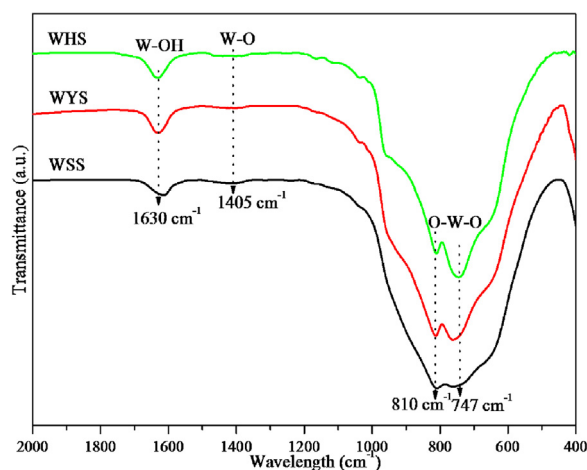


**Fig. 2.** FTIR spectra of different samples.

No.83-0950) [35,36]. No other diffraction peaks from impurities were detected, indicating all the samples were pure monoclinic phase of $WO_3$. Similar results were also observed in CWYS (see Fig. S3). Based on the XRD patterns, the crystallite size of all the $WO_3$ samples was calculated by Scherrer's equation using the (020) peaks. As shown in Table 1, it can be clearly seen that the crystallite size varied in the order of WSS > WHS > WYS = CWYS, which can be attributed to the different preparation methods.

The FTIR spectra of all the $WO_3$ samples in Fig. 2 displayed that the peak located at 1630 cm$^{-1}$ was assigned to the W-OH bending vibration mode of the adsorbed water molecules while the peak at 1405 cm$^{-1}$ corresponded to the W-O stretching vibration [30]. Meanwhile, the peaks located at 810 cm$^{-1}$ and 747 cm$^{-1}$ could be ascribed to the O—W—O stretching mode and no peaks for impurities were observed. These results confirmed that all the samples were present in pure monoclinic phase of $WO_3$, which was in good compliance with the XRD results.

The FESEM images in Fig. 3 revealed that all the $WO_3$ samples were present in uniform hierarchical microspheres with controllable interior structures from solid, yolk-shell, to hollow for WSS, WYS, and WHS, respectively, and the uniform microspheres with an average diameter were around 3.0 um. Meanwhile, their corresponding high-magnification FESEM images demonstrated that these microspheres were constructed by self-assembly of numerous interconnected nanosheets with a smooth surface, which could be further verified by the crushed sample of CWYS (see Fig. S4).
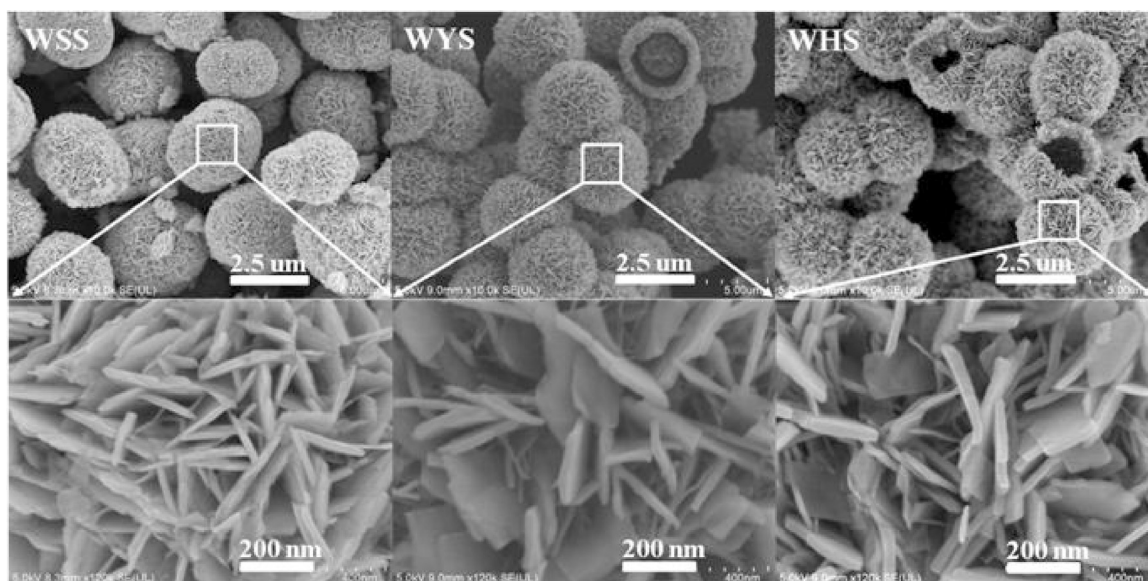


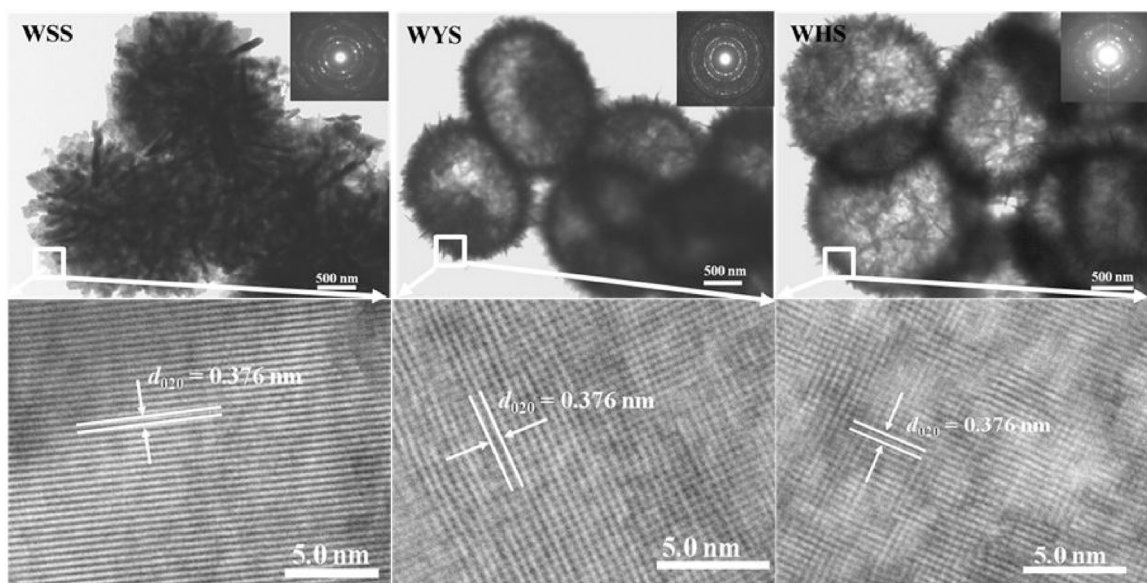**Fig. 3.** FESEM images and their selected local magnification images of different samples.

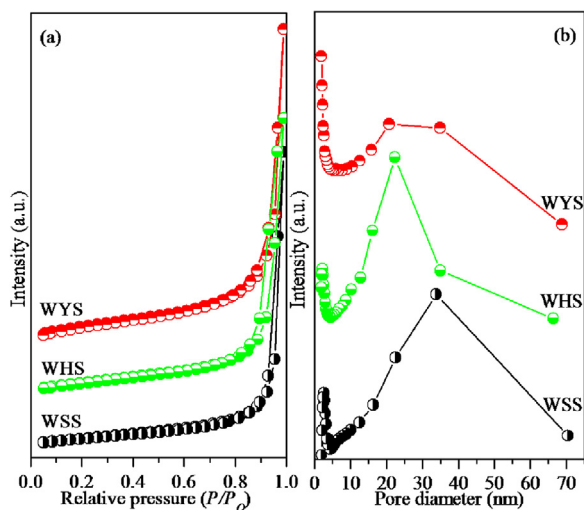**Fig. 4.** TEM and HRTEM images of different samples, and the insets are the corresponding SAED images.



**Fig. 5.** $N_2$ adsorption-desorption isotherms (a) and pore size distribution curves (b) of different samples.



**Fig. 6.** Photocurrent responses of different samples.

These $WO_3$ nanosheets were about 300 nm in length, 180 nm in width, and 40 nm in thickness, which were densely interconnected and formed a highly porous architecture. The TEM images in Fig. 4 further confirmed the above characterized results about the morphology and microstructure of all the $WO_3$ samples, and the SAED images also revealed that all the $WO_3$ samples owned the polycrystalline structures with high crystallization degree. Moreover, the interplanar spacing of lattice fringe in HRTEM images was 0.376 nm, corresponding to the (020) plane in a monoclinic $WO_3$ structure [33–36], which was good consistent with the XRD analysis.

Fig. 5 showed that all the $WO_3$ samples exhibited the typical type IV $N_2$ adsorption-desorption isotherms with H3 hysteresis loop in the relative pressure ($P/P_0$) range from 0.8 to 1.0 according to the IUPAC classification [22,40,49], indicating the presence of slit-shape pores that were generally associated with sheet-like particles, which agreed well with their interconnected nanosheets as revealed by FESEM and TEM characterizations. Meanwhile, all the $WO_3$ samples displayed high adsorption at high $P/P_0$ range and no saturated adsorption was reached until $P/P_0 = 1.0$, implying the formation of large mesopores and macropores. These obser-
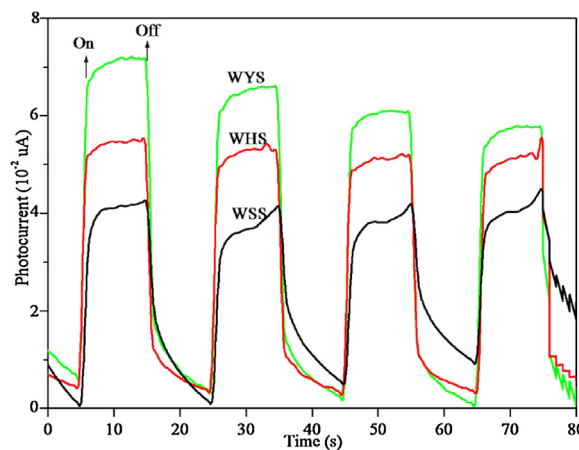
vations were further confirmed by their corresponding pore size distribution curves, in which a wide pore size distribution from mesoporous to macroporous region could be found, which was mainly formed by self-assembly of the interconnected nanosheets. Similar results were also observed in CWYS (see Fig. S5). Based on the $N_2$ adsorption-desorption isotherms, the $S_{BET}$, $V_P$, and $D_P$ of all the $WO_3$ samples have been calculated by using BET and BJH models, respectively. From Table 1, it could be clearly seen that the WYS displayed higher surface area than those of WHS and WSS, respectively, and its crushed sample of CWYS exhibited a slight higher surface area than WYS owning to the structural collapse of the yolk-shell structure. A relatively large surface area of WYS might provide more active sites for the adsorption of reactant molecules and also promote the light harvesting, making the photocatalytic process more efficient.

Fig. 6 demonstrated that all the $WO_3$ samples generated a photocurrent under light irradiation with full wavelengths, which then decayed rapidly to zero when the light irradiation was turned off, indicating that all the $WO_3$ samples acted as semiconductors to produce photoelectrons under light irradiation. Obviously, the photocurrent intensity varied in the order of WYS > WHS > WSS. Taking into account the fact that all the $WO_3$ samples were present in pure monoclinic phase with nearly the same intrinsic band gap
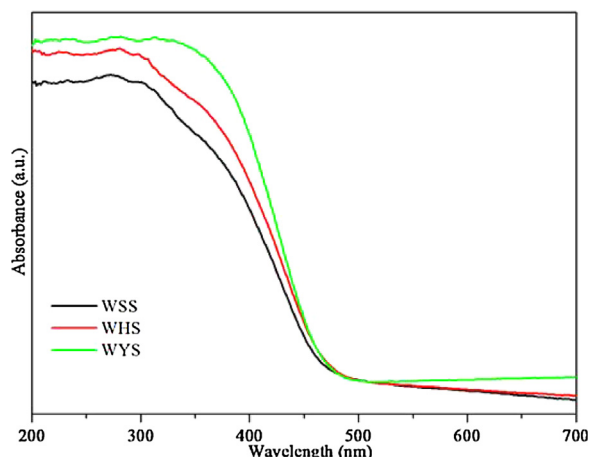
**Fig. 7.** UV–vis DRS spectra of different samples.



**Fig. 9.** PLS spectra of different samples.

(2.6 eV), the photocurrent intensity was mainly dependent on the light-harvesting ability and the separation efficiency between photoelectrons and holes. On the one hand, the UV–vis DRS spectra in Fig. 7 exhibited that all the $WO_3$ samples showed almost the same absorption profile with a steep absorption edge around 477 nm, corresponding to the intrinsic band gap of 2.6 eV characteristic of monoclinic $WO_3$ [35,36]. However, it can be clearly seen that the light absorbance in the range of 200–478 nm varied in the order of WYS > WHS > WSS, which could be ascribed to the following two aspects: one is the surface area of all the $WO_3$ samples was present in the order of WYS > WHS > WSS, which was well agreement with the photocurrent intensity, suggesting that the large surface area enlarged the contact area between photocatalysts and lights and thus promoted the light harvesting [7,14]. The other is that, since the WSS with solid interior structure only allowed the light reflections among the interconnected nanosheets, the WYS and WHS with yolk-shell and hollow structures not only allowed the light reflections among the interconnected nanosheets, but also remarkably facilitated the multiple light reflections in the yolk-shell and hollow chambers especially the yolk-shell structure as illustrated in Fig. 8, which also enhanced the light harvesting [22,41–46]. This could be further confirmed by the crushed microspheres of CWYS with similar surface area to WYS, which obviously demonstrated lower light harvesting than WYS owing to the structural collapse of yolk-shell architecture (see Fig. S6). On the other hand, the PLS spectra in Fig. 9 displayed that the intensity of PL emission peak around 740 nm decreased in the order of WSS > WHS > WYS, corresponding to the decrease in the recombination rate between photoelectrons and holes. This can be attributed to the different crystallite sizes for WSS, WHS, and WYS, respectively, and the
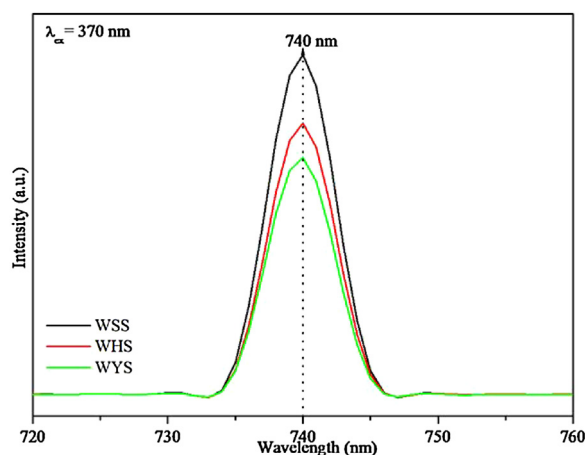
smaller crystallite size facilitated the rapid transfer of photoelectrons, which diminished the transfer distance of photoelectrons and thus inhibited their recombination with holes [7,9,46]. Therefore, it can be concluded that the unique yolk-shell structure with smaller crystallite size effectively reduced the recombination rate between photoelectrons and holes, and thus increased the number of photocharges available for photoreactions on the photocatalyst surfaces.

### 3.2. Photocatalytic performance

Selective oxidation of alcohols to carbonyl compounds such as aldehydes and ketones has been considered as one of the most important functional group transformations in industrial chemistry [1–4]. Compared with traditional organic reactions, photocatalytic selective oxidation can be carried out in aqueous medium under mild conditions without using toxic oxidizing agents, which could save energy and prevent environmental pollution [5–9]. As a typical example, the photocatalytic selective oxidation of benzyl alcohol to its corresponding benzyldehyde was firstly studied over WYS, and blank experiments demonstrated that no measurable amounts of oxidation products for benzyl alcohol occurred in the absence of either light irradiation or the WYS photocatalyst. The HPLC–MS revealed that no measurable side-products were detected, suggesting that the absolute selectivity toward the target product under the present conditions. The underlying photocatalytic reaction mechanism was investigated by the controlled experiments using various active species scavengers. As shown in Fig. 10, it can be seen that only a little decrease in photocatalytic activity was found when the terephthalic acid was added into the reaction process to capture ·OH radicals, implying that •OH radicals were not the main
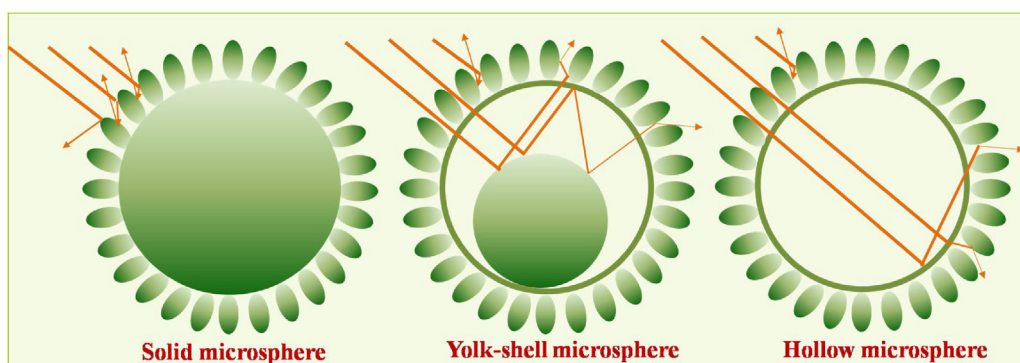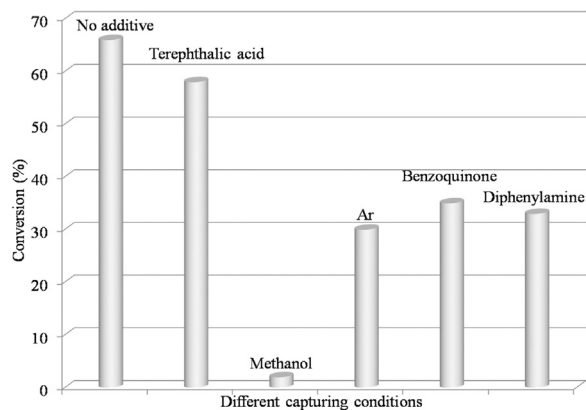


**Fig. 8.** Schematic illustration of multiple light reflections in different samples.

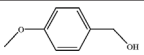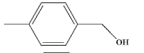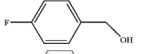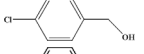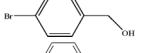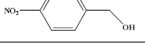**Fig. 10.** Photocatalytic performances of WYS for the selective oxidation of benzyl alcohol in the presence of different capturers.

**Table 2**
Photocatalytic performances of different samples in selective oxidation of benzylic alcohols.

| Reactant | Conversion (%) | | | |
|---|---|---|---|---|
| | WSS | WYS | WHS | CWYS |
| (structure) | 39 | 100 | 71 | 59 |
| (structure) | 34 | 86 | 65 | 55 |
| (structure) | 15 | 67 | 47 | 40 |
| (structure) | 15 | 61 | 37 | 37 |
| (structure) | 14 | 54 | 32 | 29 |
| (structure) | 10 | 49 | 26 | 21 |

active species involved in the photocatalytic oxidation [50]. However, a great decrease in the photocatalytic activity was observed by adding either methanol to capture photogenerated holes ($h^+$), or benzoquinone to capture $•O_2^-$ radicals, or diphenylamine to capture photoelectrons ($e^-$), or bubbling Ar to eliminate the dissolved $O_2$ [7,8,22]. These results provided the powerful evidences that the photogenerated holes ($h^+$), photoelectrons ($e^-$), and $•O_2^-$ radicals were mainly acted as the active species in the present photocatalytic oxidation reaction except for ·OH radicals. Based on the above results, a tentative reaction mechanism can be proposed and briefly described in Fig. 11. Firstly, the $WO_3$ semiconductor generated photoelectrons ($e^-$) and holes ($h^+$) under light irradiation via multiple reflections. Secondly, the photogenerated holes ($h^+$) activated the absorbed benzyl alcohol to produce benzyl alcohol cation radicals and the photoelectrons ($e^-$) activated the dissolved $O_2$ to form the $•O_2^-$ radicals. Finally, the benzyl alcohol cation radicals reacted with the $•O_2^-$ radicals to produce benzyldehyde.

The photocatalytic activity of selective oxidation of benzyl alcohol to benzyldehyde for all the $WO_3$ samples was shown in Fig. 12, which ranked in the order of WYS > WHS > CWYS > WSS. Meanwhile, Table 2 also revealed that all the $WO_3$ samples exhibited the same sequence in photocatalytic selective oxidation of benzylic alcohols to their corresponding aldehydes. Thus, the WYS was determined as the optimal photocatalyst in the present reactions, which displayed the highest photocatalytic activity. This superior photocatalytic activity of WYS can be attributed to the synergistic promoting effect of the following factors: firstly, the WYS

with porous structure constructed by self-assembly of interconnected nanosheets together with higher surface area facilitated the adsorption and diffusion of reactant molecules, and also enlarged the contact area between photocatalysts and lights and thus promoted the light harvesting. Secondly, the WYS with smallest crystallite size naturally diminished the transfer distance of photoelectrons and thus, reduced their recombination rate with holes [7]. Thirdly, the hierarchical yolk-shell structure possessed unique advantages, *e.g.* the shells made the reactant molecules and products diffuse rapidly through the shells, and the hollow space between the core and the shell could provide a large surface area and a confined homogenous environment for photocatalytic reaction, which increased the contact time between photocatalysts and reactant molecules [38]. Importantly, the yolk-shell structure favored more multiple light reflections within the interior cavity than those of hollow and solid microspheres, respectively, allowing more efficient use of light source and therefore offering a greatly improved photocatalytic activity. Taking into account the fact that the WYS and its crushed sample of CWYS had the same crystallization degree and similar surface area, but the CWYS showed a dramatically decreased activity, which could further verify that the yolk-shell structure enhanced the light harvesting via multiple reflections. Moreover, the special photoactivity of different samples in Table 1 also manifested that the yolk-shell structure played the key role in determining the photocatalytic activity under present conditions owning to that the WYS exhibited nearly three and two times higher photoactivity than those of
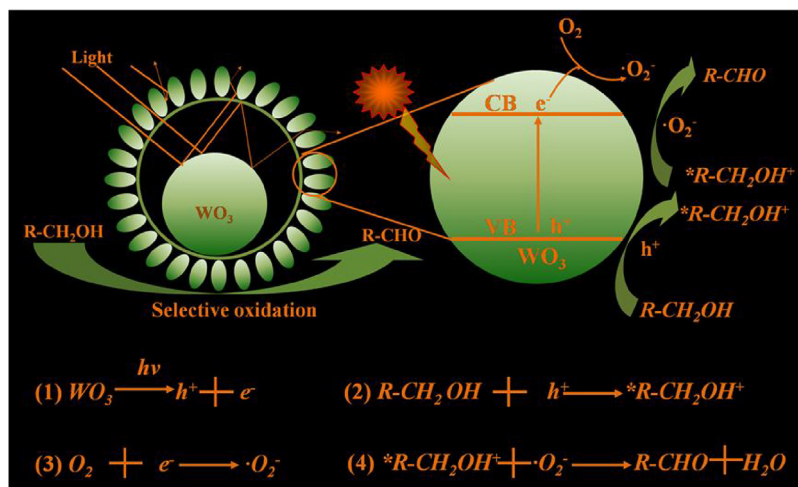


**Fig. 11.** A plausible mechanism for photocatalytic selective oxidation of aromatic alcohols to their corresponding aldehydes.
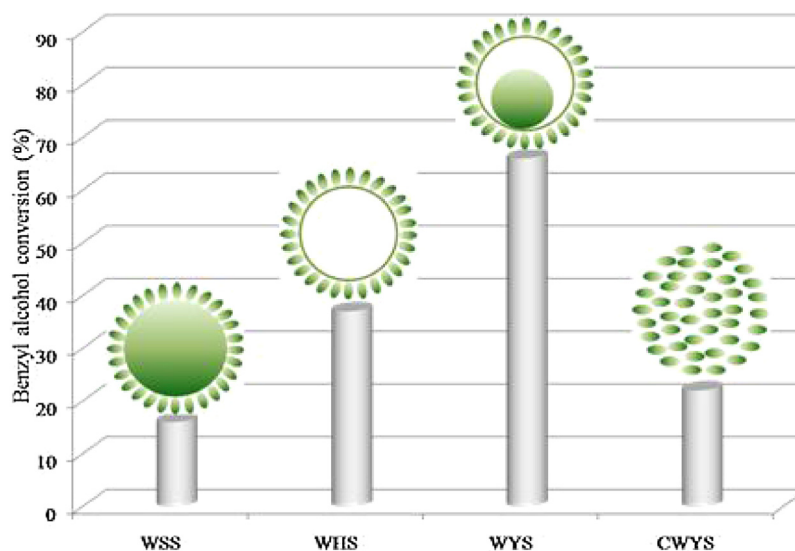
**Fig. 12.** Photocatalytic activity of different samples for the selective oxidation of benzyl alcohol.
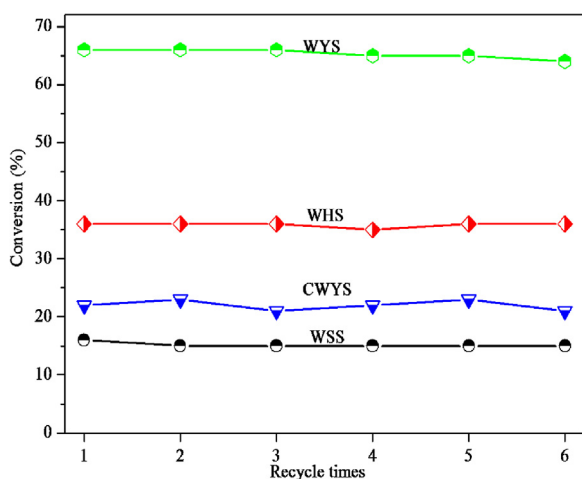


**Fig. 13.** Recycling test of different samples for the selective oxidation of benzyl alcohol.

WSS and WHS, respectively. From Table 2, we can clearly see that benzylic alcohols with electron-donating groups (*e.g. p-CH₃* and *p-OCH₃*) demonstrated higher conversion than those with electron-withdrawing groups (*e.g. p-F, p-Cl, p-Br,* and *p-NO₂*), which was in good compliance with our previous works [7–9]. This can be attributed to that the electron-donating groups endowed the -$CH_2OH$ moieties with higher electron cloud density than those with electron-withdrawing groups and thus, the photogenerated holes more easily reacted with -$CH_2OH$ to produce the corresponding cation radicals, which also confirmed the rationality of photocatalytic mechanism as proposed in Fig. 11.

The durability is one of the key criteria for a photocatalyst in practical applications. To explore the durability of all the WO₃ samples, the photocatalyst was allowed to centrifuge after each run of reactions, followed by washing thoroughly with distilled water and absolute ethanol. Then, the photocatalyst was reused by charging fresh reactants for the subsequent recycle of photocatalytic reaction under the identical reaction conditions. As shown in Fig. 13, it can be clearly seen that all the WO₃ samples could be reused for at least six times without notable deactivation, indicating the high and strong durability of all the WO₃ samples. This excellent durability can be ascribed to their robust hierarchical architectures against structural collapse, which has been verified by FESEM images (see

Fig. S7) since the morphological structures of all the WO₃ samples almost kept intact after the 6th recycle.

## 4. Conclusions

In summary, we have successfully synthesized hierarchical synthesized WO₃ microspheres with controllable interior structures from solid, yolk-shell, to hollow, which are highly active and selective for photocatalytic selective oxidation of aromatic alcohols in aqueous medium under light irradiation with full wavelengths. The yolk-shell WO₃ microspheres exhibited superior photocatalytic activity due to the porous structure together with high surface area, the yolk-shell structure and the small crystallite size, which could facilitate the adsorption and diffusion of reactant molecules, enhance the light harvesting *via* multiple reflections in yolk-shell chambers, and inhibit the recombination rate between photoelectrons and holes. Meanwhile, all the WO₃ photocatalysts displayed excellent durability against structural collapse due to the robust hierarchical structures. Our work might guide the future rational design of highly efficient photocatalysts with unique hierarchical architectures for practical applications.

## Appendix A. Supplementary data

Supplementary data associated with this article can be found, in the online version, at http://dx.doi.org/10.1016/j.apcatb.2017.07.027.

# References

[1] D.I. Enache, J.K. Edwards, P. Landon, A.A. Herzing, M. Watanabe, C.J. Kiely, D.W. Knight, G.J. Hutchings, Science 311 (2006) 362–365.
[2] Y.B. Kuang, N.M. Islam, Y. Nabae, T. Hayakawa, M. Kakimoto, Angew. Chem. Int. Ed. 49 (2010) 436–440.
[3] C. Aellig, C. Girard, I. Hermans, Angew. Chem. Int. Ed. 50 (2011) 12355–12360.
[4] X.C. Wu, S.W. Guo, J.Y. Zhang, Chem. Commun. 51 (2015) 6318–6321.
[5] G. Palmisano, V. Augugliaro, M. Pagliarob, L. Palmisano, Chem. Commun. 43 (2007) 3425–3437.
[6] Q. Wang, M. Zhang, C.C. Chen, J.C. Zhao, Angew. Chem. Int. Ed. 49 (2010) 7976–7979.
[7] J.G. Wang, Z.F. Bian, J. Zhu, H.X. Li, J. Mater. Chem. A 1 (2013) 1296–1302.
[8] X.R. Li, J.G. Wang, Y. Men, Z.F. Bian, Appl. Catal. B 187 (2016) 115–121.
[9] J.G. Wang, P.H. Rao, W. An, Y. Men, Appl. Catal. B 195 (2016) 141–148.
[10] H.X. Qin, Y.Y. Bian, Y.X. Zhang, L.F. Liu, Z.F. Bian, Chin. J. Chem. 35 (2017) 203–208.
[11] M.C. Wen, Y. Kuwahara, K. Mori, D.Q. Zhang, H.X. Li, H. Yamashita, J. Mater. Chem. A 3 (2015) 14134–14141.
[12] M.C. Wen, Y.W. Cui, Y. Kuwahara, K. Mori, H. Yamashita, ACS Appl. Mater. Interfaces 8 (2016) 21278–21284.
[13] M.C. Wen, K. Mori, Y. Kuwahara, H. Yamashita, ACS Energy Lett. 2 (2017) 1–7.
[14] J.G. Wang, P. Zhang, X. Li, J. Zhu, H.X. Li, Appl. Catal. B 134–135 (2013) 198–204.
[15] C. Tang, L.F. Liu, Y.L. Li, Z.F. Bian, Appl. Catal. B 201 (2017) 41–47.
[16] Y. Kuwahara, H. Yamashita, J. Mater. Chem. 21 (2011) 2407–2416.
[17] K. Peramaiah, V. Ramalingam, M.C. Wen, H. Yamashita, B. Neppolian, RSC Adv. 50 (2015) 39752–39759.
[18] Y.L. Li, Y.Y. Bian, H.X. Qin, Y.X. Zhang, Z.F. Bian, Appl. Catal. B 206 (2017) 293–299.
[19] L.Z. Wang, T. Sasaki, Chem. Rev. 114 (2014) 9455–9486.
[20] G. Liu, H.G. Yang, J. Pan, Y.Q. Yang, G.Q. Lu, H.M. Cheng, Chem. Rev. 114 (2014) 9559–9612.
[21] M. Pelaeza, N.T. Nolan, M.H. Entezarig, D.D. Dionysiou, Appl. Catal. B 125 (2012) 331–349.
[22] J.G. Wang, X.R. Li, X.i Li, J. Zhu, H.X. Li, Nanoscale 5 (2013) 1876–1881.
[23] R. Asahi, T. Morikawa, H. Irie, T. Ohwaki, Chem. Rev. 114 (2014) 9824–9852.
[24] M. Dahl, Y.D. Liu, Y.D. Yin, Chem. Rev. 114 (2014) 9853–9889.
[25] Y. Peng, K.K. Wang, T. Liu, J. Xu, B.G. Xu, Appl. Catal. B 203 (2017) 946–954.
[26] F. Vaquero, R.M. Navarro, J.L. Fierro, Appl. Catal. B 207 (2017) 93–102.
[27] T. Cai, Y. Liu, L.L. Wang, S.Q. Zhang, C.B. Liu, S.L. Luo, Appl. Catal. B 208 (2017) 1–13.
[28] Y.N. Huo, M. Miao, Y. Zhang, J. Zhu, H.X. Li, Chem. Commun. 47 (2011) 2089–2091.
[29] J.G. Wang, F.L. Cao, Z.F. Bian, K.H. Leung, H.X. Li, Nanoscale 6 (2014) 897–902.
[30] W.Y. Zhu, F.Q. Sun, R. Goei, Y. Zhou, Appl. Catal. B 207 (2017) 93–102.
[31] Y.B. Shen, W. Wang, X.X. Chen, B.Q. Zhang, S.L. Gao, B.Y. Cui, J. Mater. Chem. A 4 (2016) 1345–1352.
[32] B.W. Ma, J.F. Guo, W.L. Dai, K.N. Fan, Appl. Catal. B 123–124 (2012) 193–199.
[33] D.Q. Zhang, S.L. Wang, J. Zhu, H.X. Li, Y.F. Lu, Appl. Catal. B 123–124 (2012) 398–404.
[34] J. Ding, L. Zhang, Q. Liu, W.L. Dai, G.F. Guan, Appl. Catal. B 203 (2017) 335–342.
[35] J.Q. Yan, T. Wang, G.J. Wu, W.L. Dai, N.J. Guan, L.D. Li, J.L. Gong, Adv. Mater. 27 (2015) 1580–1586.
[36] D.J. Ham, A. Phuruangrat, S. Thongtem, J.S. Lee, Chem. Eng. J. 165 (2010) 365–369.
[37] H.Y. Liu, H. Ma, J. Joo, Y.D. Yin, Sci. China Mater. 59 (2016) 1017–1026.
[38] W.J. Dong, Y.J. Zhu, H.D. Huang, C.R. Li, B.Y. Chen, Z. Shi, G. Wang, J. Mater. Chem. A 1 (2013) 10030–10036.
[39] Y.T. Wang, J.M. Cai, Y. Tian, T. Ding, J.L. Gong, Z. Jiang, X.G. Li, ACS Appl. Mater. Interfaces 8 (2016) 23006–23014.
[40] S.X. Wang, X.J. Yang, Y.P. Wang, L.X. Liu, Y.Y. Guo, H. Guo, J. Solid State Chem. 213 (2014) 98–103.
[41] H.X. Li, Z.F. Bian, J. Zhu, D.Q. Zhang, G.S. Li, Y.N. Huo, H. Li, Y.F. Lu, J. Am. Chem. Soc. 129 (2007) 8406–8407.
[42] Z.F. Bian, J. Zhu, F.L. Cao, Y.N. Huo, Y.F. Lu, H.X. Li, Chem. Commun. 46 (2010) 8451–8453.
[43] J. Zhu, S.H. Wang, J.G. Wang, D.Q. Zhang, H.X. Li, App. Catal. B 102 (2011) 120–125.
[44] G.Z. Liao, S. Chen, X. Quan, Y.B. Zhang, H.M. Zhao, Appl. Catal. B 102 (2011) 126–131.
[45] G.L. Li, G. Li, J. Li, G.B. Jiang, Catal. Sci. Technol. 6 (2016) 3108–3116.
[46] Z.F. Bian, J. Zhu, H.X. Li, J. Photochem. Photobiol. C 28 (2016) 72–86.
[47] S.L. Bai, K.W. Zhang, L.S. Wang, J.H. Sun, D.Q. Li, A.F. Chen, J. Mater. Chem. A 2 (2014) 7927–7934.
[48] W.X. Wang, X.H. Meng, K. Zhang, P. Li, D.C. Choi, J.H. Park, Y.K. Son, Electrochim. Acta 215 (2016) 466–472.
[49] H. Tong, Y.M. Xu, X.L. Cheng, X.F. Zhang, S. Gao, H. Zhao, L.H. Huo, Electrochim. Acta 210 (2016) 147–154.
[50] S.B. Zhu, T.G. Xu, H.B. Fu, J.C. Zhao, Y.F. Zhu, Environ. Sci. Technol. 41 (2007) 6234–6239.